

# NLTE Stellar Population Synthesis of Globular Clusters using Synthetic Integrated Light Spectra I: Constructing the IL Spectra

Mitchell. E. Young

Department of Astronomy & Physics and Institute for Computational Astrophysics, Saint Mary's University, Halifax, NS, Canada, B3H 3C3

`myoung@ap.smu.ca`

C. Ian Short

Department of Astronomy & Physics and Institute for Computational Astrophysics, Saint Mary's University, Halifax, NS, Canada, B3H 3C3

Received \_\_\_\_\_; accepted \_\_\_\_\_

## ABSTRACT

We present an investigation of the globular cluster population synthesis method of McWilliam & Bernstein (2008), focusing on the impact of NLTE modeling effects and CMD discretization. Johnson-Cousins-Bessel U-B, B-V, V-I, and J-K colors are produced for 96 synthetic integrated light spectra with two different discretization prescriptions and three degrees of NLTE treatment. These color values are used to compare NLTE and LTE derived population ages. Relative contributions of different spectral types to the integrated light spectra for different wavebands are measured. Integrated light NLTE spectra are shown to be more luminous in the UV and optical than LTE spectra, but show stronger absorption features in the IR. The main features showing discrepancies between NLTE and LTE integrated light spectra may be attributed to light metals, primarily Fe I, Ca I, and Ti I, as well as TiO molecular bands. Main Sequence stars are shown to have negligible NLTE effects at IR wavelengths compared to more evolved stars. Photometric color values are shown to vary at the millimagnitude level as a function of CMD discretization. Finer CMD sampling for the upper main sequence and turnoff, base of the red giant branch, and the horizontal branch minimizes this variation. Differences in ages derived from LTE and NLTE IL spectra are found to range from 0.55 to 2.54 Gyr, comparable to the uncertainty in GC ages derived from color indices with observational uncertainties of 0.01 magnitudes, the limiting precision of the Harris catalog (Harris 1996).

*Subject headings:* Galaxy: globular clusters: general — stars: atmospheres, fundamental parameters — techniques: photometric

## 1. INTRODUCTION

Because of their old ages, relative homogeneity of their populations, and high luminosities, globular clusters (GCs) can be used to study the chemical evolution history of galaxies. The most luminous GCs presumably only trace the major star forming events, including mergers. Even basic metallicity provides interesting information for comparison with the Galaxy. However, the detailed chemical composition of GCs could potentially provide much more information on galaxy evolution, because the chemical elements are produced by a variety of stars, with varying sensitivity to stellar mass and metallicity. High resolution spectroscopic chemical abundance analysis of individual stars in Galactic GCs has long been pursued (Cohen 1978; Pilachowski, Canterna, & Wallerstein 1980). Such abundance studies are a useful tool for probing the chemical evolution of the Galaxy (Snedden *et al.* 1991; Briley, Smith, & Lambert 1994). Unfortunately, similar studies have not been possible outside of the Milky Way, as individual stars cannot be resolved in distant galaxies.

For extragalactic GCs, cluster metallicities have been estimated using broadband photometric colors (Forte, Strom, & Strom 1981; Geisler, Lee, & Kim 1996) and low-resolution integrated light (IL) spectra (Racine, Oke, & Searle 1978; Brodie & Huchra 1990). Results from such studies include the discovery of bimodal GC metallicity and color distributions in extragalactic systems (Elson & Santiago 1996; Whitmore *et al.* 1995) reminiscent of the bimodal GCs in the Milky Way (Zinn 1985).

In recent years, stellar population synthesis (SPS) of GC populations has provided a new avenue of investigating the chemical composition of either spatially resolved or unresolved GCs, provided high spectral-resolution IL spectra can be obtained (McWilliam & Bernstein 2008; Colucci *et al.* 2009, 2011). Using both broadband photometric colors and equivalent

widths (EWs) of spectroscopic absorption lines as diagnostics, detailed information on the chemical composition of a cluster as a whole can be derived.

Non-local thermodynamic equilibrium effects have been demonstrated to be present in the spectra of asymptotic-giant branch (AGB) stars in the Galactic GCs 47 Tuc (Lapenna *et al.* 2014), affecting the analysis of Fe I and II abundances. While the same effects have yet to be demonstrated in red-giant branch (RGB) GC stars, there is a possibility that the effects will be reflected in the IL spectra of a cluster if it is present in its brightest members.

### 1.1. Present Work

Our primary goal is to investigate NLTE modeling effects on the IL spectra of synthetic GCs, as well as ages and metallicities subsequently derived from them, using the population synthesis methodology presented by McWilliam & Bernstein (2008). We test two degrees of NLTE treatment, one where we model only the component of the population more evolved than the sub-giant branch in NLTE, and the other where we model the entire population in NLTE. We also investigate the uncertainty associated with the color-magnitude diagram (CMD) discretization used in this method. We compare ages for synthetic clusters derived from photometric colors of both LTE and NLTE spectra, and we assess the significance of deviations caused by NLTE effects by comparing them to those caused by photometric uncertainty.

## 2. LIBRARY OF SYNTHETIC SPECTRA

We used PHOENIX v.15 to compute spherically symmetric model atmospheres and high resolution synthetic spectra ( $R \approx 300000$ ) for stars that cover the CMD parameter

spaces of GCs at various ages and metallicities spanning Galactic values. We produced a library of stellar atmospheres covering the ranges of  $T_{\text{eff}} = 3000$  to  $15000$  K (in steps of 200 K below  $T_{\text{eff}} = 4000$  K, 1000 K above  $T_{\text{eff}} = 10000$  K, and 250 K otherwise) and  $-0.5$  to  $5.0$  dex in  $\log g$  (in steps of 0.5 dex) (Coelho 2014). Figure 1 shows the extent of the coverage in  $T_{\text{eff}}$  vs  $\log g$  space. This coverage was reproduced for three values of metallicity,  $[M/H] = -1.49, -1.00,$  and  $-0.66,$  and two values of stellar mass,  $M = 0.5$  and  $1.0 M_{\odot}.$

Our library was built in two halves, “warm” stars and “cool” stars, using a separate pipeline for each. For cool star models, we consider 47 different molecules, with a combined total of 119 isotopologues and isotopomers, in both the equation of state (E.O.S.) and opacity calculations. The molecules taken into consideration are listed in Table 1. The atmospheres are also left to naturally form convection zones. For warm star models, we do not consider molecules in the E.O.S. or opacity calculations. Molecules are fully dissociated in stars earlier than F0, which Cox (2000) lists as  $T_{\text{eff}} \gtrsim 7300$  K; we choose to err on the side of including molecules unnecessarily and include them in models with  $T_{\text{eff}} \leq 7500$  K, to ensure they are present in all models where they are significant. We also take this as the  $T_{\text{eff}}$  value above which the possibility of convection is no longer considered in our models, treating the whole extent of the atmosphere as if it were in radiative equilibrium. The one exception to this division of warm and cool stars is modeling the linear Stark broadening of H I lines. We include the broadening in the spectra of atmospheres with  $T_{\text{eff}} \geq 5000$  K; spectra cooler than this do not have significant Stark wings on H I features.

All of our atmospheric models have alpha enhanced abundances, with  $\alpha = +0.4$  dex. For our initial solar composition, we take our abundances up to O from Grevesse, Noels, & Sauval (1996), and take the revised abundances of Scott *et al.* (2015a) (F to Ca), Scott *et al.* (2015b) (Sc to Ni), and Grevesse *et al.* (2015) (Cu to Cs). We

assume values for microturbulent velocities of  $\xi = 4 \text{ km s}^{-1}$  for stars of  $\log g = 3.0$  and lower, and  $\xi = 1 \text{ km s}^{-1}$  for stars of  $\log g = 3.5$  and higher. Two distinct values are used here instead of a more realistic continuous variation to artificially enhance the distinction between spectral lines dominated by evolved and unevolved populations in the IL spectrum.

The synthetic spectral output of PHOENIX is the monochromatic flux spectral energy distribution (SED) of a model atmosphere, measured at an optical depth surface of  $\tau_{12000} = 0$ . Each synthetic spectrum in our library needs to be scaled by a factor of  $(R_{\tau=0}/R_{\tau=1})^2$ , where the radii are obtained from the corresponding structural models, to convert to the flux spectrum at the  $\tau_{12000} = 1$  surface. This provides consistency between models of equivalent  $T_{\text{eff}}$  that have varying values of  $\log g$ . We sample our spectra over the wavelength range  $\lambda = 2000$  to  $27000 \text{ \AA}$  at a spectral resolution of  $R = 300000$ , allowing us to compare values of cluster parameters derived from UV (Bellini *et al.* 2015; Piotto *et al.* 2015) and IR (Cohen *et al.* 2015; Valcheva *et al.* 2015) photometry, to those derived from more traditional optical photometry and spectroscopy.

## 2.1. NLTE Atmospheres

In this work, we explore the effects of NLTE atmospheric modeling on synthetic IL spectra and cluster ages and metallicities derived from them. The atmospheric structures and synthetic spectra are self-consistently modeled in NLTE. We focus on NLTE modeling because Fe I line strengths and EWs in an IL spectrum are the main diagnostic features for deriving cluster parameters (McWilliam & Bernstein 2008), and Fe I is one of the atomic species most heavily affected by NLTE in synthetic spectra.

### 2.1.1. NLTE Model Atoms

Because we study NLTE effects on GC parameters derived from IL spectra, the accuracy and completeness of our NLTE treatment is an important concern. It was shown by Mashonkina *et al.* (2011) that using a more complete Fe I atomic model will reduce NLTE overionization effects by providing more high energy excited states to facilitate recombination from Fe II. They found that the greater the number of energy levels within  $\Delta E = kT_{\text{eff}}$  of the ground state ionization energy ( $\chi_{\text{Ion}}$ ), the more accurate the NLTE ionization equilibrium solution.

To this end, we have adopted a set of new and updated NLTE model atoms, that are improved with respect to Young & Short (2014). These new atoms generally add to the numbers and refine the exact atomic data values of the energy levels and transitions over the old model atoms. Table 2 shows a comparison of the numbers of levels and lines between the old and new model atoms. In addition to the species listed in the table, H I, He I, and Ne I are also treated in NLTE, but are handled internally by PHOENIX and have not been updated. However, in the cases of He I and Ne I, these species do not dominate massive line blanketing, while the old H I treatment is sufficiently complete to model the asymptotic convergence of the Balmer series lines for rounding out the Balmer jump. For details on the NLTE treatment of these species, see Young & Short (2014).

These new model atoms provide a significant improvement for some species, such as Fe I and II. Specifically, for Fe I, the new model atom has nearly double the number of energy levels, and more than triple the number of b-b transitions than the old. Additionally, the difference between the highest energy level and  $\chi_{\text{ion}}$  in the old Fe I model atom was  $\Delta E = 0.322eV$ , which meant that stars cooler than  $T_{\text{eff}} \sim 3750 K$  would not have any energy levels within  $kT_{\text{eff}}$  of  $\chi_{\text{ion}}$ . With the new model atom, there are now 45 energy levels

closer to  $\chi_{\text{ion}}$ , and for the coolest stars in our library at  $T_{\text{eff}} = 3000 \text{ K}$ , 17 energy levels are within  $kT_{\text{eff}}$  of  $\chi_{\text{ion}}$ .

### 3. SYNTHETIC COLOR MAGNITUDE DIAGRAMS

#### 3.1. Isochrones

For this work, we have employed the Teramo theoretical isochrones, from the BaSTI group (Pietrinferni *et al.* 2006). The Teramo isochrones are offered with a variety of theoretical assumptions made in calculating the stellar evolutionary tracks, including alpha-enhanced or scaled solar compositions, with or without convective core overshooting, two different mass-loss rates following the Reimers Law, and normal or extended AGBs. The isochrones cover ranges of -3.27 to 0.51 dex in metallicity and 30 Myr to 19 Gyr in age. Each one is sampled at 2000 mass points with a variable sampling frequency to ensure that each area of the CMD is critically sampled. The 30 Myr isochrones cover a range of initial masses from 0.5 to 8.5  $M_{\odot}$ , with the upper mass limit being reduced for isochrones with greater ages as stars evolve beyond the modeled tip of the AGB. The mass sampling frequency is increased for these isochrones to maintain the 2000 sampling points.

We select a subset of isochrones to investigate, with alpha enhancement of  $\alpha = +0.4$ , mass loss parameter  $\eta = 0.2$ , normal AGBs, and without core overshoot, similar to the selection of Colucci *et al.* (2009). We focus our investigation on those isochrones with ages and metallicities covering the range of observed Galactic GC values, spanning 9 to 15 Gyr and  $[M/H] = -1.49$  to  $-0.66$  dex. These values were chosen as the isochrone metallicities closest to the peak values of the metal-rich and metal-poor Galactic GC populations (Zinn 1985). We extend our ages beyond the range of average Galactic values (10-13 Gyr), to investigate the possible size of the effect NLTE modeling can have on derived ages.



The isochrones include stars mapping out the transition from the tip of the RGB to the red end of the HB. We remove these stars before populating our CMD for two reasons: 1) This transition is not well understood theoretically; and 2) Including these stars would interfere with our CMD discretization procedure, outlined below in Section 4.1. When included in a population, these stars contribute  $< 1\%$  of the total cluster luminosity, and have a negligible impact on the IL SED.

### 3.2. Initial Mass Function

To expand the isochrones into full populations, we use Kroupa’s initial mass function (IMF) (Kroupa 2001), normalized as a probability density function of the form

$$p_{\text{Kroupa}}(m) = \begin{cases} Ak_0 m^{-0.3} & 0.01 M_\odot < m < m_1 \\ Ak_1 m^{-1.3} & m_1 < m < m_2 \\ Ak_2 m^{-2.3} & m_2 < m < m_3 \\ Ak_3 m^{-2.3} & m_3 < m \end{cases} \quad (1)$$

with  $k_0 = 1$ ,  $k_1 = k_0 m_1^{-0.3+1.3}$ ,  $k_2 = k_1 m_2^{-1.3+2.3}$ , and  $k_3 = k_2 m_3^{-2.3+2.3}$  ensuring a continuous function, where  $m_1 = 0.08 M_\odot$ ,  $m_2 = 0.50 M_\odot$ , and  $m_3 = 1.00 M_\odot$  (Maschberger 2012).  $A$  is a global normalization constant. This form gives information about the relative frequencies of stars of various masses as opposed to the number of stars of different masses in a unit spatial volume.

The normalization constant,  $A$ , is determined for each isochrone individually, relative to their respective mass sampling ranges. To get the relative frequencies of the stars in each isochrone independently, we take a continuous mass range and divide it into bins centered on the isochrone points, with bin divisions halfway between adjacent points. The IMF is

then numerically integrated over these bins using the extended trapezoid rule to get the relative frequency for each.

### 3.3. Populating the CMDs

To build our synthetic populations, we take a given target luminosity for the population,  $L_{\text{tot}}$ , representative of the luminosity of a real cluster, and analytically allocate fractions of  $L_{\text{tot}}$  to the isochrone points according to the relative frequencies. This determines the total luminosity of each point and, when divided by a point’s individual luminosity, the number of stars representing that point in the population. This can result in non-whole numbers of stars for each isochrone point.

There is no intrinsic spread of CMD features or observational scatter from any source inherent in the synthetic population of our CMDs; they are built as simple stellar populations out of single isochrones. We choose not to introduce any spread or scatter in the population artificially. This is unnecessary, as any random variations introduced will be averaged away in the creation of the IL spectrum, outlined in Section 4.2.

## 4. SYNTHETIC INTEGRATED LIGHT SPECTRA

The integrated light spectrum of a globular cluster is the combined light of every individual star within the cluster. Since it is not feasible to model hundreds of thousands of stars for each cluster that is to be studied, even when interpolating within a library of stellar models, a method by which an IL spectrum can be approximated is necessary.

#### 4.1. Discretizing the CMD

We choose to represent groups of parametrically similar stars in a GC CMD by a single stellar spectrum per group and weight their contributions to the IL spectrum, following the method of McWilliam & Bernstein (2008). The method involves discretizing a CMD by binning parametrically similar stars areas bounded by lines of constant  $T_{\text{eff}}$  and  $L_{\text{Bol}}$ . These areas, or boxes, are established such that an approximately equal fraction of the total cluster luminosity is emitted by the stars contained in each. McWilliam & Bernstein (2008) limit the luminosity contained in any box to  $\sim 3$  to  $4$  % of the total luminosity for a given cluster ( $\sim 25$  to  $30$  boxes total); we choose to increase the total number of boxes to  $50$  ( $\sim 2$  % of  $L_{\text{tot}}$  each), effectively doubling the discretization resolution in our CMDs. This prevents the boxes from covering too large a range of values of the stellar parameters, which ensures that a single representative stellar spectrum will be an accurate approximation of the integrated spectrum for a box.

Starting at the low-mass end of the main sequence, stars of increasing mass are added to a box until the sum of their luminosities matches the allotted percentage of the total cluster luminosity for a box. The box is then considered full and subsequent stars are added to a new box. The process is repeated for increasing stellar mass until everything up to the tip of the RGB is enclosed in a box. We repeat the process starting at the low-mass end of the HB and proceed up the AGB, until the entire population has been placed into boxes. The process is explicitly broken and restarted here to avoid too large of a box from encompassing both the RGB tip and HB by blindly adding stars of increasing masses to boxes. This effectively splits our CMD into two components by ignoring short lived and poorly understood stars in the transition from the RGB to the HB. The first component is comprised of the main sequence, sub-giant branch, and red giant branch (the MR component), while the second encompasses the asymptotic giant and horizontal branches

(the HA component). Figure 2 shows an example of a theoretical population similar in age and metallicity to 47 Tuc (age = 13.06 Gyr,  $[M/H] = -0.78$ ) (Forbes & Bridges 2010), including the discretization boxes.

To determine the number of boxes necessary to properly sample the CMD, while maintaining approximately equal luminosity for each box, we calculate the ratio of the luminosity of the MR component ( $L_{MR}$ ) to that of the HA component ( $L_{HA}$ ). We then iterate through a total number of boxes, as well as the numbers of boxes allotted to each component, finding the optimal combination to be the one where the ratio of MR boxes ( $N_{MR}$ ) to HA boxes ( $N_{HA}$ ) most closely matches the ratio of luminosities. By limiting the total number of boxes to between 25 and 50, this combination gives the closest agreement between

$$\frac{L_{MR}}{N_{MR}} \sim \frac{L_{HA}}{N_{HA}}$$

maintaining approximately equal luminosity in each box, while still limiting each box to 2 to 4 % of the total cluster luminosity.

## 4.2. Creating the Representative Stars

Once the CMD discretization is completed, we proceed to calculate the atmospheric modeling parameters for a representative star in each box. To produce a synthetic spectrum for this box star, we require  $T_{\text{eff}}$ ,  $\log g$ ,  $[M/H]$ , and either  $M$  or  $R$ . Metallicity is constant along each isochrone, and prescribes the value for a box star directly. As we are interested in representing the combined light of every star in a box with a single stellar spectrum, we take the average of the parameters over a whole box, weighted by

$$w_* = N_* / N_{\text{box}}$$

the fractional number of stars of each isochrone mass sampling bin per box.

The  $T_{\text{eff}}$  of our box star is found from

$$\langle T_{\text{eff}} \rangle = \langle w_* * T_{\text{eff},*}^4 \rangle^{1/4}$$

where the values for individual stars,  $T_{\text{eff},*}$ , are taken directly from the isochrones. We take the average of the fourth power, rather than a linear average, to include the relative contribution each star makes to the total luminosity of a box. Similarly, the average mass and luminosity can be found from

$$\langle M \rangle = \langle w_* * M_* \rangle$$

$$\langle L_{\text{bol}} \rangle = \langle w_* * L_{\text{bol},*} \rangle$$

where once again, the individual quantities are taken directly from the isochrones.

There is some ambiguity in calculating the average  $\log g$  for a box. Because  $\log g$  is not a stellar interior modeling parameter, it is not included directly in the isochrones, so a direct average is unavailable in this case. We choose to take the averages of the relevant isochrone quantities and calculate a single  $g$  from those average values,

$$\langle g \rangle = \frac{G \langle M \rangle 4\pi \sigma \langle T_{\text{eff}}^4 \rangle}{\langle L \rangle}$$

without calculating individual  $g$  values for the isochrone sampling points. This method has the benefit of being consistent with the reverse process of observers inferring parameters from the IL spectrum of a group of spatially unresolved stars.

### 4.3. Synthesizing IL Spectra

Now that the full CMD distribution has been reduced to the representative stars, we generate stellar spectra for each box by interpolating among synthetic spectra in our

library. We linearly interpolate our library spectra weighted by three or four atmospheric modeling parameters;  $T_{\text{eff}}$ ,  $\log g$ ,  $M$ , and, in cases where the isochrone value is not a direct match to one of the values in our library,  $[M/H]$ . This interpolation scheme results in each box spectrum being formed by interpolating among either 8 (matching library  $[M/H]$ ) or 16 (interpolating  $[M/H]$ ) individual spectra from our library. We chose to interpolate using a linear method because our library is already pushing the lower boundaries of atmospheric structure convergence in  $T_{\text{eff}}$  and  $\log g$ , and higher order methods would require additional synthetic spectra with even lower values for these parameters. We test the accuracy of this interpolation by comparing two IL spectra generated using this procedure (one interpolating linear flux spectra and one interpolating log flux spectra) to one generated from synthetic spectra with the exact parameters of the representative stars. Figure 3 shows that there is relatively little difference between our interpolated and exact IL spectra, except for the shortest wavelengths that we model, and that there is little appreciable difference between interpolating linear or log fluxes. Representative populations for the youngest and oldest isochrones in this study are plotted in Figure 1 as a visual indication of where the interpolation between library spectra will occur for  $T_{\text{eff}}$  and  $\log g$ .

In nature, IL spectra are combinations of the luminosity spectra of individual stars, not the flux spectra. Because of this, we must convert our box representative spectra from PHOENIX surface fluxes to luminosities. The most direct method of doing so takes advantage of

$$\frac{L_{\lambda}}{F_{\lambda}} = \frac{L_{\text{bol}}}{F_{\text{bol}}}$$

where  $L_{\text{bol}}$  for a box is the average value as calculated above, and we calculate the  $F_{\text{bol}}$  by numerically integrating low resolution PHOENIX spectra from 10 to 10,000,000 Å using the extended trapezoid rule, ensuring sufficient coverage of both the Wien side and Rayleigh-Jeans tail of the spectra.

We now combine the box spectra into a synthetic IL spectrum. Each spectrum is scaled by

$$L_{\lambda,box} = N_{box} * L_{\lambda}$$

to account for the total luminosity of the box, and then added together. Three IL spectra per CMD are created this way; one composed of LTE stellar spectra, one of NLTE stellar spectra, and one composed of both LTE and NLTE stellar spectra where only the evolved population were NLTE. For our purposes, we consider any star more evolved than the sub-giant branch to be “evolved”. These hybrid IL spectra allow us to isolate and study the impact NLTE modeling of the evolved population has on cluster parameters inferred from IL spectra. The LTE and NLTE spectra for our 47 Tuc population are overplotted for comparison in Figure 4, with the absolute and relative NLTE-LTE differences, to highlight the most disparate spectral features.

Identifying the atomic and molecular species responsible for the large differences between the LTE and NLTE spectra is not a straightforward task when dealing with IL spectra. Because an IL spectrum is the co-added light of multiple spectra of different spectral types, what appears to be a single feature in the IL spectrum may be caused by multiple sources of opacity. Additionally, at the modest spectral resolution of Figure 4, blending of features in crowded regions can confuse the issue even further. To proceed with IL feature identification, we take five sample stars from our library models ( $T_{\text{eff}} = 6500$  K and  $\log g = 4.5$ ,  $T_{\text{eff}} = 5750$  K and  $\log g = 3.5$ ,  $T_{\text{eff}} = 5000$  K and  $\log g = 3.0$ ,  $T_{\text{eff}} = 4250$  K and  $\log g = 2.0$ ,  $T_{\text{eff}} = 3600$  K and  $\log g = 0.5$ ), and identify the sources of any large discrepancies between the sample NLTE and LTE spectra. We weight a NLTE-LTE difference in the spectrum of a sample star by that star’s relative contribution to the IL luminosity in the photometric band corresponding to the wavelength of that difference. Figure 5 displays an example of these relative contributions for the 15.0 Gyr population. If the discrepancies

in the sample stars are also found to be present in the IL spectrum, the sources in the individual spectra are considered to be responsible. The species responsible for the majority of large differences were found to be primarily light metals in their ground states, Fe I being the most prominent among these, with a few exceptions. The large deviation observed in the range from  $\lambda \approx = 4000$  to  $8500 \text{ \AA}$  was identified as TiO molecular bands from our cool giant stars. The clusters of lines seen in the range  $\lambda \approx = 10000$  to  $12000 \text{ \AA}$  were Ti I, and the strong lines near  $\lambda \approx = 19000$  to  $20000 \text{ \AA}$  were found to be Ca I. A full set of high resolution diagnostics will be included in a forthcoming paper in this series.

## 5. PHOTOMETRIC ANALYSIS & RESULTS

To take an initial estimate of the magnitude of the effect NLTE modeling has on parameters derived from IL spectra, we examine four photometric color indices (U – B, B – V, V – I, and J – K) produced using Bessel’s updated Johnson-Cousins UBVRI photometric system (Bessel 1990) as well as Bessel and Brett’s VJHKLL’M photometric system (Bessel 1988). We analyze a collection of IL spectra for synthetic CMDs approximating 47 Tuc, with  $[M/H] = -0.66$  and substituting  $M_v = -8.64$  for  $L_{\text{tot}}$ , except ranging in age from 9 to 15 Gyr. Two sets of these spectra are generated, each using the LTE, NLTE, and hybrid prescriptions, limiting the number of boxes to 25 to 35 (set 1) and 40 to 50 (set 2). Synthetic photometric colors for these IL spectra are single-point calibrated to both a NLTE synthetic spectrum approximating Vega ( $T_{\text{eff}} = 9600 \text{ K}$ ,  $\log g = 4.1$ ,  $[M/H] = -0.5$ ), and the library spectrum that most closely approximates Arcturus ( $T_{\text{eff}} = 4250 \text{ K}$ ,  $\log g = 2.0$ ,  $[M/H] = -0.66$ ). Arcturus was chosen for this second calibration to compare the IL colors to that of a standard star that is representative of the populations. We denote color values calibrated to each star as  $X - Y_{\text{Vega}}$  and  $X - Y_{\text{Arc}}$  respectively.



### 5.1. Colors and Ages

Figures 6 and 7 present the values of the color indices as a function of population age for sets 1 and 2 respectively, highlighting the NLTE - LTE differences. Qualitatively, there is little difference between the two sets. All four color indices display a reddening of IL color as the population ages, as more of the population evolves into older, cool stars. The NLTE colors for the first three color indices are bluer than LTE at all ages, because NLTE overionization of Fe I weakens the myriad weak Fe I lines that have the character of a pseudo-continuous opacity in the blue and near UV bands. Conversely, the J – K NLTE colors are redder than LTE, where the surplus of free electrons produced by the overionization increases  $H^-$  opacity in the J band ( $< 1.6 \mu\text{m}$ ). The NLTE-LTE color differences for the indices in both sets are consistent with a constant value as a function of age, with the exception of U – B, where the difference is seen to increase as a function of age.

The hybrid color values fall midway between the LTE and NLTE colors for the UV and optical indices, and converge with the NLTE values at IR wavelengths. There are two possible explanations for this convergence: 1) Evolved stars dominate the IL spectra in these filters' wavebands; and 2) NLTE effects in main sequence stars negligible in these wavebands. To determine which of the two effects is responsible for the convergence, we refer back to the representative stars' relative luminosity contributions in Figure 5. As can be seen for V – I, evolved stars do not dominate the IL spectrum, with all representative stars making approximately equal contributions to the IL spectrum in the I band, and the main sequence stars near the turnoff are the strongest contributors in the V band. In this case, it would suggest that negligible NLTE effects in main sequence stars at these wavelengths are responsible for the observed convergence of hybrid to NLTE colors. For J – K, the same explanation is likely responsible, but a combination of the two effects is

also possible. For both the J and K bands, evolved stars on the red giant branch are the strongest contributors to the IL spectrum (although they do not dominate it).

To give a quantitative estimate for how much of an impact NLTE effects in IL spectra have on derived ages, we first define the quantity  $\Delta_{\text{Age}}$ , the uncertainty in derived age from the uncertainty in measured color index value, such that

$$\Delta_{\text{Age}} = \Delta_{\text{color}} \frac{dA(\text{color})}{d(\text{color})}$$

where  $\Delta_{\text{color}}$  is the numerical uncertainty of a given color value, and  $A(\text{color})$  describes the derived cluster age as a function of “observed” color value, found by parameterizing the IL color vs age relation with a low order polynomial. We find that a linear function does not provide a good match to the relation, but a parabola provides an excellent match for all color indices, with coefficients of determinations of at least  $R^2 \geq 0.997$ . We contrast these  $\Delta_{\text{Age}}$  values with the difference between the NLTE and LTE derived ages for a given color,  $A_{\text{color,NLTE}} - A_{\text{color,LTE}}$ . The full list of  $\Delta_{\text{Age}}$  values and the differences in NLTE and LTE derived ages for all color indices are presented in Table 3. For comparison, we also present the uncertainty in derived ages found from setting  $\Delta_{\text{color}}$  equal to 0.01 mag, the limiting precision of the Harris catalog (Harris 1996).

The U – B color index returned the largest differences, but these results were considered to be unrealistic for a number of reasons, including keeping the metallicity fixed throughout this experiment and the difficulty associated with modeling the near-UV region of stellar spectra. The other three indices, B – V, V – I, and J – K, produced comparable age differences, with those derived from V – I generally being the largest by  $\lesssim 40\%$ . Age differences for our B – V index ranged from 0.61 to 1.58 Gyr for set 1, and 0.55 to 2.53 Gyr for set 2. The smaller age difference for each set corresponds to the bluest color measured

for the LTE IL spectra, and the larger difference corresponds to the reddest measured LTE color. For comparison, the range of  $\Delta_{\text{Age}}$  values for  $B - V$  are 0.22 to 0.82 Gyr and 0.13 to 0.53 Gyr, for sets 1 and 2 respectively. Assuming an observational limiting precision of 0.01 mag for  $B - V$ , the limiting precision of the Harris catalog, results in  $\Delta_{\text{Age}}$  values of 1.12 to 2.41 Gyr and 1.05 to 2.84 Gyr.

We note that all of our IL spectra were produced from isochrones of fixed metallicity, and that age estimates derived in this fashion may vary greatly with changing metallicity. It should also be noted that both LTE and NLTE model atmospheres have been shown to overpredict near-UV flux in the spectra of cool giant stars (Short & Hauschildt 2009), and this will likely be reflected in the IL spectra. Any results found from fitting synthetic IL spectra to observed spectra at UV wavelengths would be impacted by this overprediction. Either or both of these effects may help explain the large differences in ages derived from our  $U - B$  colors. Additionally, this work is only concerned with a differential analysis between LTE and NLTE IL spectra, and in turn is only affected by any difference in the overpredictions. NLTE models are worse in the overprediction than their LTE counterparts as a result of NLTE Fe I overionization, but the updated Fe I NLTE model atom we have implemented should minimize this for the range of stellar parameters with which we are concerned. We also expect that, to first order, the NLTE-LTE difference in the overprediction of UV flux to be constant as a function of isochrone age.

## 5.2. Numerical Uncertainty

Figure 8 shows the  $B - V$  colors for two isochrones, ages 9 and 15 Gyr, as a function of the number of boxes used to discretize the CMD. The value of a color index for a given population varies at the millimagnitude level as a function of the CMD discretization

resolution. As might be expected, the variations are larger for lower discretization resolution, and are reduced for higher resolution. This trend is qualitatively repeated for the other color indices.

To isolate which regions of the CMD are being over- or under-sampled, we plot in Figure 9 the  $T_{\text{eff}}$  of the representative stars in three histograms, comparing the CMDs on either side of the largest change in color (ie. that between 30 and 32 boxes), and two control cases to either side of the largest change where there is relatively little change (29 to 30 boxes, and 32 to 33 boxes). The bin size for each histogram was set to 250 K, the temperature resolution of our library of spectra, and the bar heights for the four sets of representative stars (29, 30, 32, and 33 boxes) were each weighted by a factor of  $f_B/f_V$ , the flux in the B band emitted by stars in that bin divided by the flux in the V band, the influence a given bin has on the IL B – V value, and independently normalized to sum to 1. We use a reduced  $\chi^2_\nu$  statistic, listed with each panel in Figure 9, to confirm that there is a greater difference between the populations in the 30 to 32 boxes histogram than in either the 29 to 30 boxes or the 32 to 33 boxes histograms. Inspection of this histogram reveals the most significant differences between the two populations occur for  $T_{\text{eff}}$  values  $\geq 4750$  K. For our populations, this corresponds to the upper main sequence (including the turnoff), the base of the red giant branch, and the horizontal branch. Special care must be paid to these regions when discretizing the CMD to ensure they are not under-sampled.

As a measure of the numerical uncertainty in the IL spectrum resulting from CMD discretization, we evaluate the  $3\sigma$  deviations in the computed integrated B-V index as a function of the number of boxes used to discretize isochrones at several ages spanning the age range. Uncertainties for the other color indices are obtained in a similar fashion. These uncertainties are represented as the error bars in Figures 6 and 7.

## 6. SUMMARY

We have investigated a number of aspects of the method presented by Colucci *et al.* (2011), refined from that of McWilliam & Bernstein (2008), for synthesizing GC populations and IL from a library of stellar atmospheric models and spectra. Following this method, a collection of 98 IL spectra for clusters approximating 47 Tuc were generated with different CMD discretization resolutions and different degrees of NLTE treatment.

For these clusters, age estimates that may be derived by fitting observed photometric colors with synthetic LTE colors were shown to differ from those similarly obtained from NLTE modeling by up to 2.54 Gyr. These age differences, while larger than the numerical uncertainties inherent in our methodology, are comparable with the limiting observational precision of current catalogs.

Our investigation of CMD discretization resolution has shown that the IL spectrum is resolution-dependent, and that the effects on the spectrum are stronger at lower resolution. These effects are more prominent at shorter wavelengths. We also find that the 25 to 35 boxes recommended in the literature do not provide enough resolution to critically sample the upper main sequence and horizontal branch. At least 40-50 boxes are necessary to minimize the resolution dependency.

Initial analysis suggests that NLTE effects in MS stars have approximately equivalent influence on IL spectra as do those in evolved stars for UV and optical wavelengths, but negligible influence for IR wavelengths. This effect appears to be independent of CMD discretization resolution for those resolutions investigated here.

### 6.1. Future Work

Future papers in this series will be based on an expanded spectral library with a metallicity dimension that spans the range between the peaks of the bimodal distribution of Galactic GCs. We will expand the photometric analysis to include the Hubble photometric system for additional UV colors, motivated by the fact that spectral features in the UV are highly sensitive to changes in metallicity. We will investigate equivalent widths and line profiles for nearly 600 spectral lines as well as Lick indices, all identified in the literature as useful features in determining cluster metallicities, for multiple atomic species, including Fe I and II. We also plan on expanding the methodology to include identifying multiple populations within single clusters and deriving their parameters.

We would like to thank the NSERC Discovery Grant program and Saint Mary's University's Faculty of Graduate Studies and Research for funding this work. We would also like to acknowledge Compute Canada member ACENet for providing us with all computational resources and CPU time.

## REFERENCES

- Bellini, A., Renzini, A., Anderson, J., et al., 2015, *ApJ*, 805, 178-197
- Bessel, M. S., 1988, *PASP*, 100, 1134
- Bessel, M. S., 1990, *PASP*, 102, 1181
- Briley, M. M., Smith, V. V., & Lambert, D. L., 1994, *ApJ*, 424, L119-L122
- Brodie, J. P., & Huchra, J. P., 1990, *ApJ*, 362, 503-521
- Cohen, J. G., 1978, *ApJ*, 223, 487-508
- Cohen, R. E., Hempel, M., Mauro, F., et al., 2015, *AJ*, in press (arXiv:1509.01470v2)
- Coelho, P. R. T., 2014, *MNRAS*, 440, 1027-1043
- Colucci, J. E., Bernstein, R. A., Cameron, S., et al., 2009, *ApJ*, 704, 385-414
- Colucci, J. E., Bernstein, R. A., Cameron, S., et al., 2009, *ApJ*, 735, 55
- Cox, A. N., 2000, *Allen's Astrophysical Quantities* (4th ed.; New York, NY: Springer)
- Elson, R. A. W., & Santiago, B. X., 1996, *MNRAS*, 278, 617
- Forbes, D. A., & Bridges, T., 2010, *MNRAS*, 404, 1203
- Forte, J. C., Strom, S. W., & Strom, K. M., 1981, *ApJ*, 245, L9
- Geisler, D., Lee, M. G., & Kim, E., 1996, *AJ*, 111, 1529
- Grevesse, N., Noels, A., & Sauval, A. J., 1996, *ASP Conf. Ser.*, 99, 117-126
- Grevesse, N., Scott, P., Asplund, M. *et al.*, 2015, *A&A*, 573, A27
- Harris, W.E., 1996, *AJ*, 112, 1487

- Kroupa, P., 2001, MNRAS, 322, 231-246
- Lapenna, E., Mucciarelli, A., Lanzoni, B. et al, 2014, ApJ, 797, 124
- Maschberger, Th., 2012, MNRAS, 429, 1725-1733
- Mashonkina, L., Gehren, T., Shi, J.-R., et al., 2011, A&A, 528, A87
- McWilliam, A., & Bernstein, R., 2008, ApJ, 684, 326-347
- Pietrinferni, A., Cassisi, S., Maurizio, S. *et al.*, 2006, ApJ, 642, 797-812
- Pilachowski, C. A., Canterna, R., & Wallerstein, G., 1980, ApJ, 235, L21
- Piotto, G., Milone, A. P., Bedin, L. R., et al., 2015, AJ, 149, 91-118
- Racine, R., Oke, J. B., & Searle, L. 1978, ApJ, 223, 82
- Scott, P., Grevesse, N., Asplund, M. *et al.*, 2015, A&A, 573, A25
- Scott, P., Asplund, M., Grevesse, N. *et al.*, 2015, A&A, 573, A26
- Short, C. I., Hauschildt, P. H., 2009, ApJ, 691, 16341647
- Snedden, C., Kraft, R. P., Prosser, C. F., et al., 1991, AJ, 102, 2001
- Valcheva, A. T., Ovcharov, E. P., Lalova, A. D., et al., 2015, MNRAS, 446, 730-736
- Whitmore, B. C., Sparks, W. B., Lucas, R., et al., 1995, ApJ, 454, L73
- Young, M. E. & Short, C. I., 2014, ApJ, 787, 43-55
- Zinn, R., 1985, ApJ, 293, 424-444



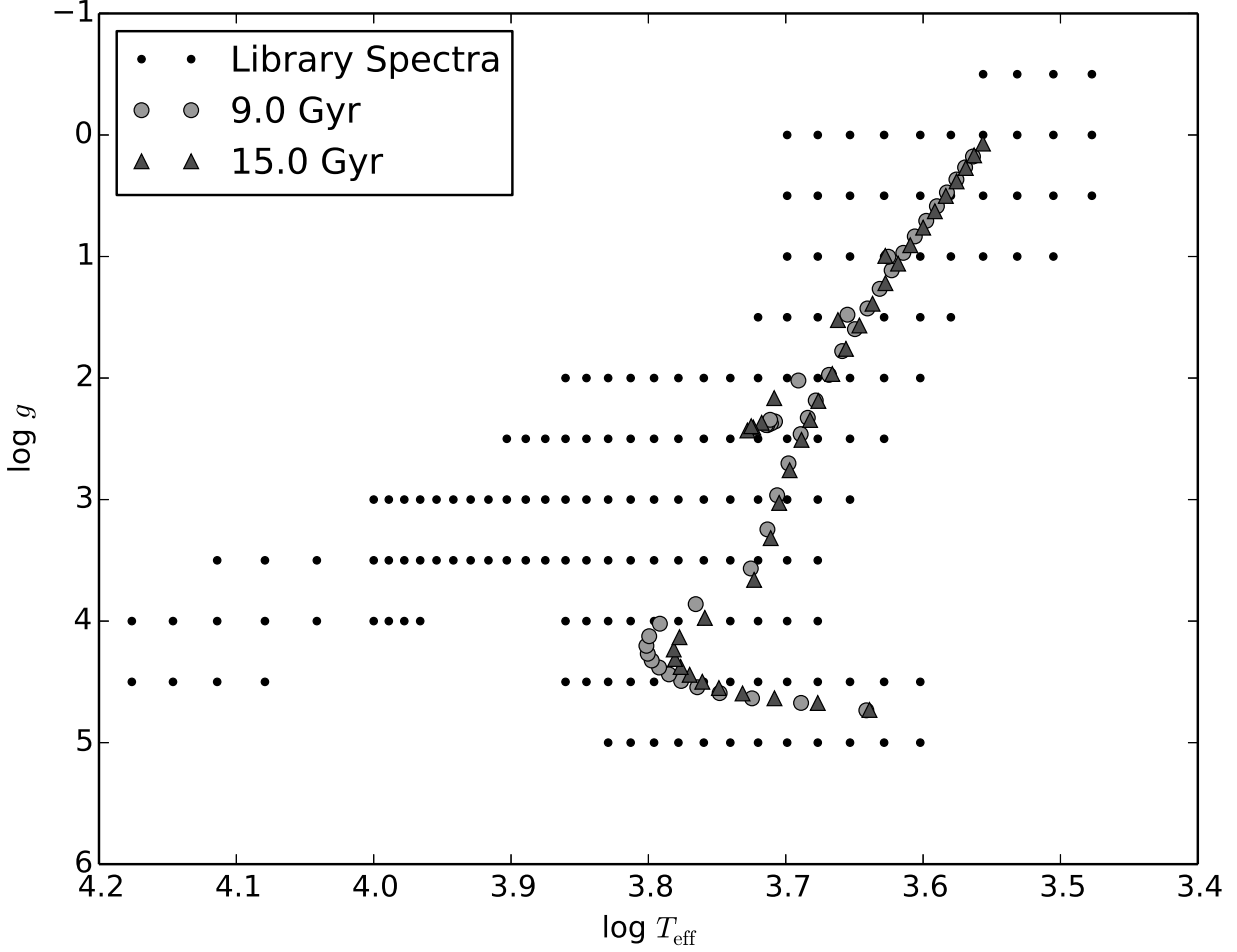


Fig. 1.— Coverage of our library of stellar atmospheres and spectra in  $T_{\text{eff}}$  vs  $\log g$  space. This selection is reproduced at both  $0.5$  and  $1 M_{\odot}$  and at each of  $[M/H] = -0.66, -1.0,$  and  $-1.49$ . Two sample representative populations produced from the  $9.0$  and  $15.0$  Gyr isochrones have been plotted to indicate where library interpolation occurs.

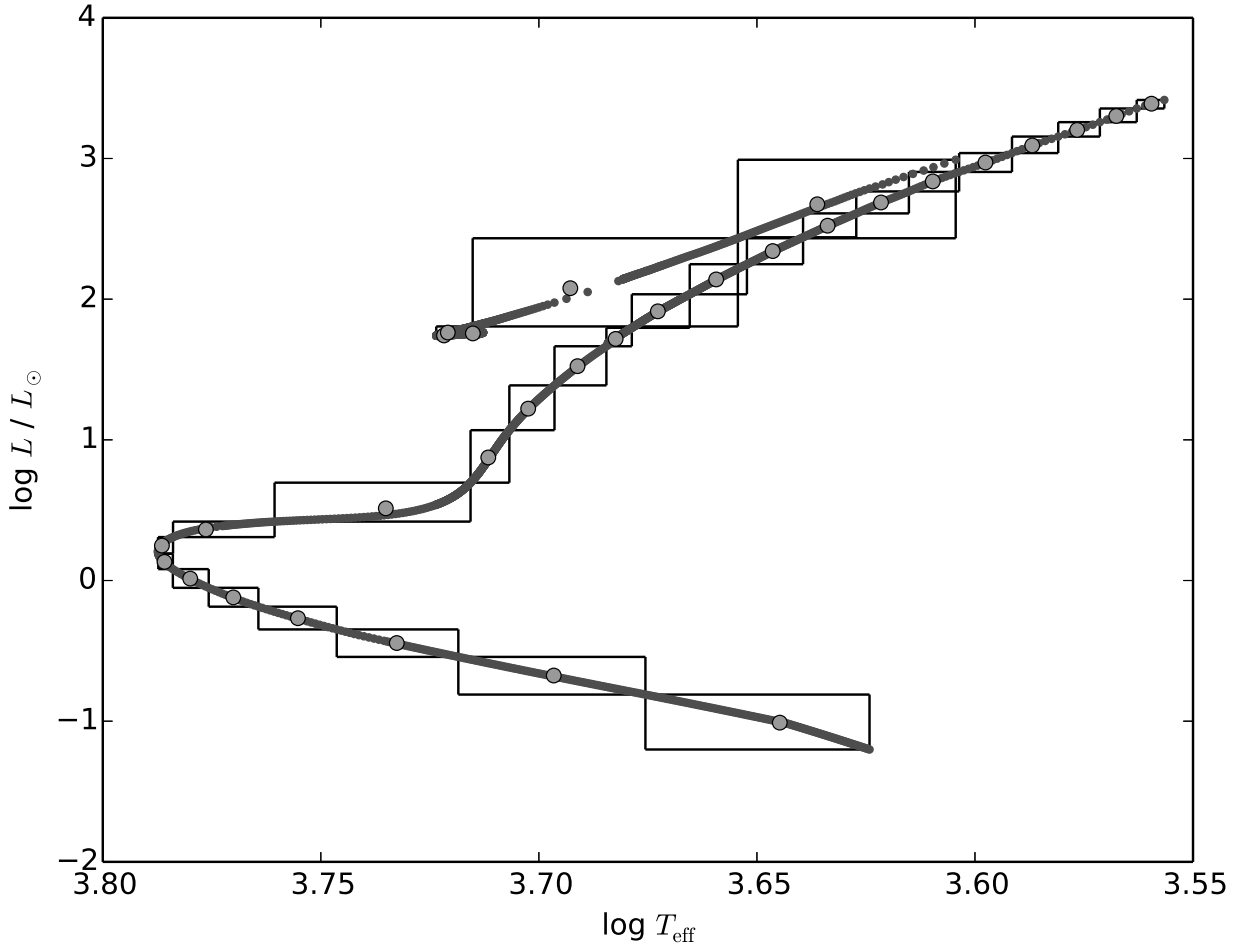


Fig. 2.— CMD of a sample population similar to 47 Tuc (age = 13.0 Gyr,  $[M/H] = -0.66$ ). The black outlines are our CMD discretization “boxes”, the dark gray points are isochrone sampling points, and the light gray circles are box representative average stars.

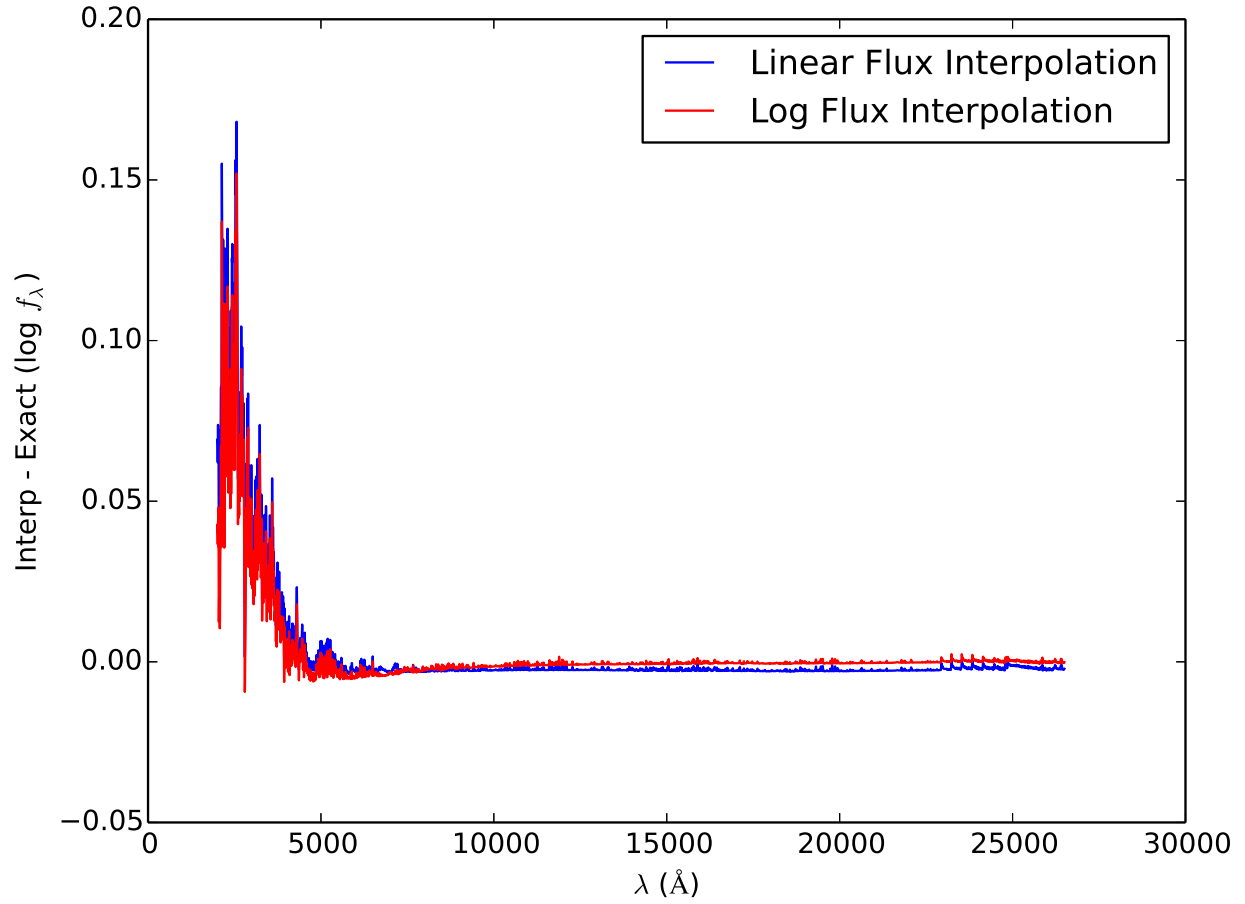


Fig. 3.— The differences between IL spectra generated by interpolating library spectra and an IL spectrum generated from spectra with the exact parameters of the representative stars. *Blue* - Linear interpolation of linear fluxes. *Red* - Linear interpolation of log fluxes.

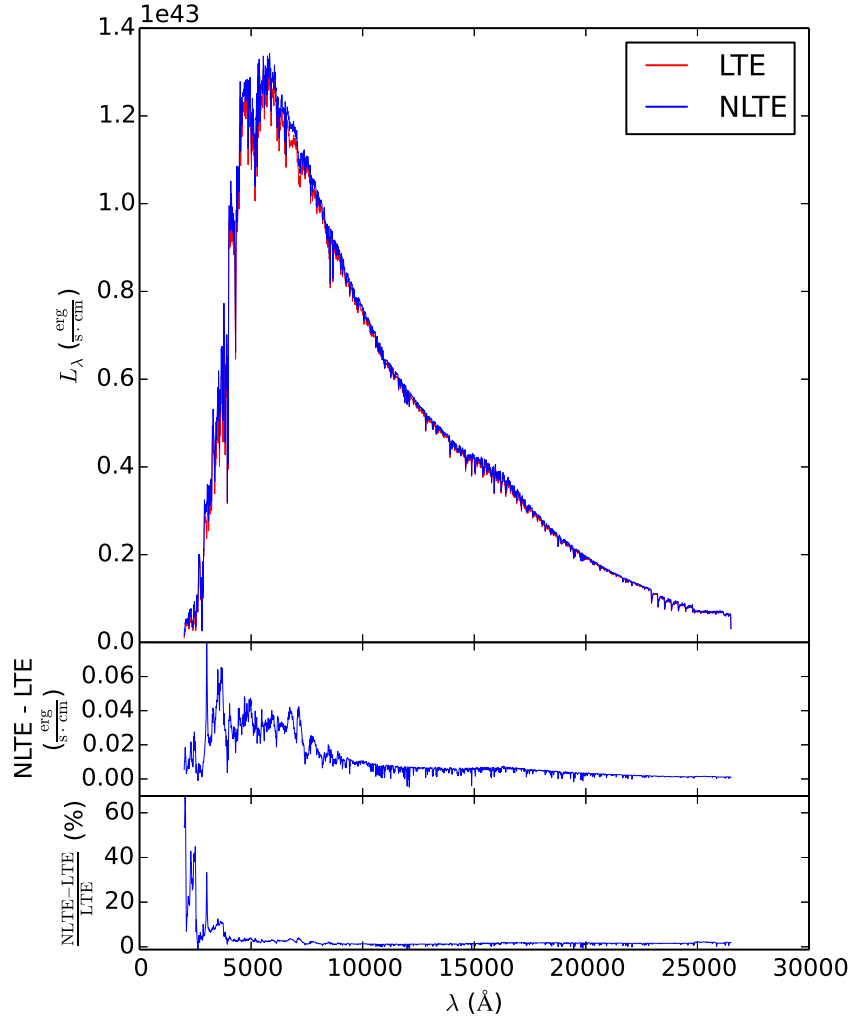


Fig. 4.— Comparison of NLTE and LTE IL spectra for the population of Figure 2. The species responsible for the majority of discrepancies between the spectra are light metals, primarily Fe I, with a few exceptions. The large deviation observed in the range from  $\lambda \approx 4000$  to  $8500 \text{ \AA}$  is caused by TiO molecular bands. The clusters of lines seen in the range  $\lambda \approx 10000$  to  $12000 \text{ \AA}$  are those of Ti I, and the strong lines near  $\lambda \approx 19000$  to  $20000 \text{ \AA}$  are those of Ca I. All three panels have been convolved from our high resolution spectra to a spectral resolution of  $R \sim 5000$  for ease of viewing. *Top* - Synthetic IL spectra for the population of Figure 2. *Middle* - Absolute difference between NLTE and LTE synthetic IL spectra. The NLTE spectrum is more luminous in the UV than LTE, while showing stronger absorption features in the IR. *Bottom* - Relative difference between NLTE and LTE synthetic IL spectra.

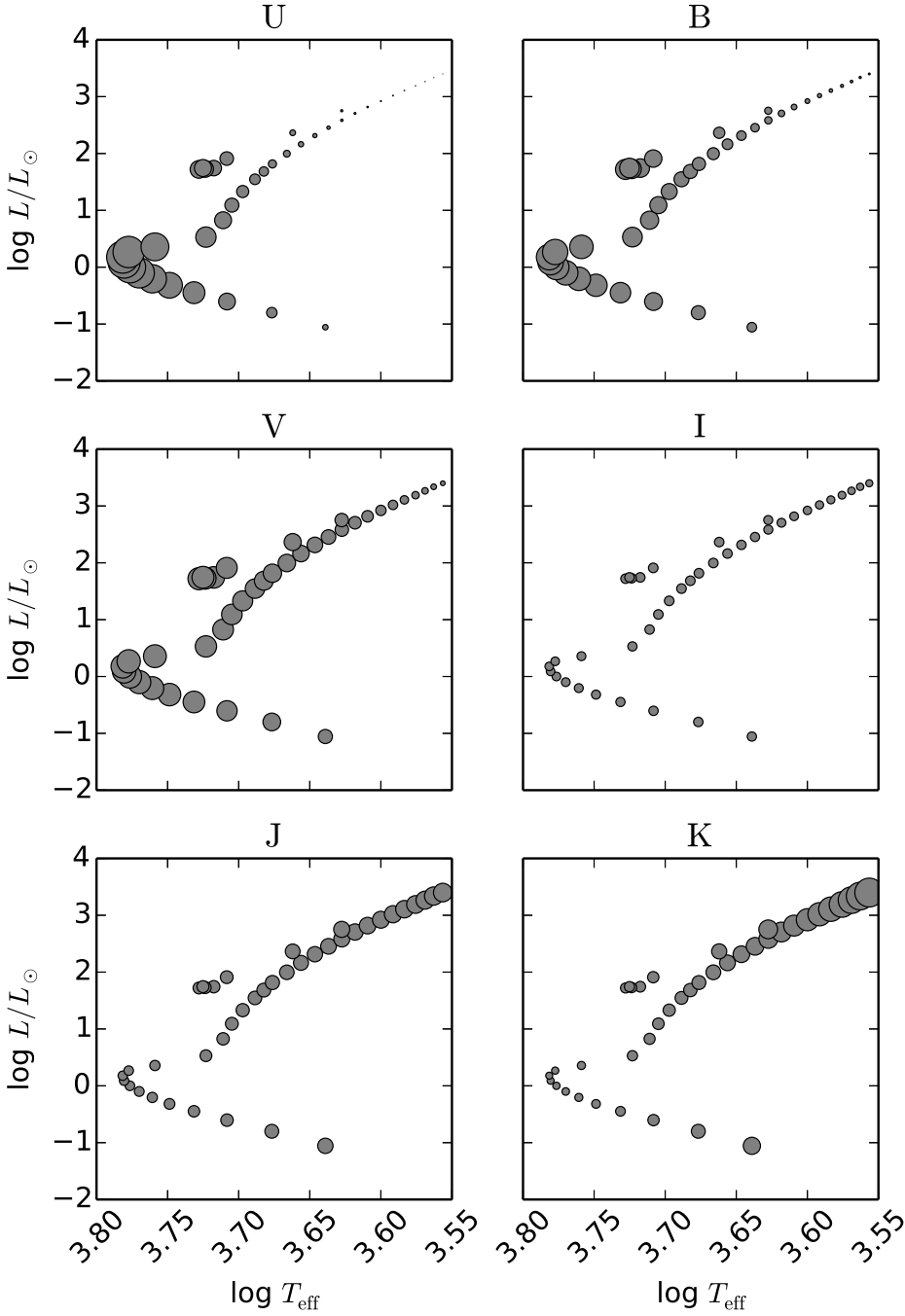


Fig. 5.— CMDs of the 15.0 Gyr population representative stars, displaying each star’s relative contribution to the IL spectrum in select photometric bandpasses. For each filter, the radius of each circle is scaled to the percentage of the total IL flux in that band contributed by the star. Circle sizes are not correlated across different filters.

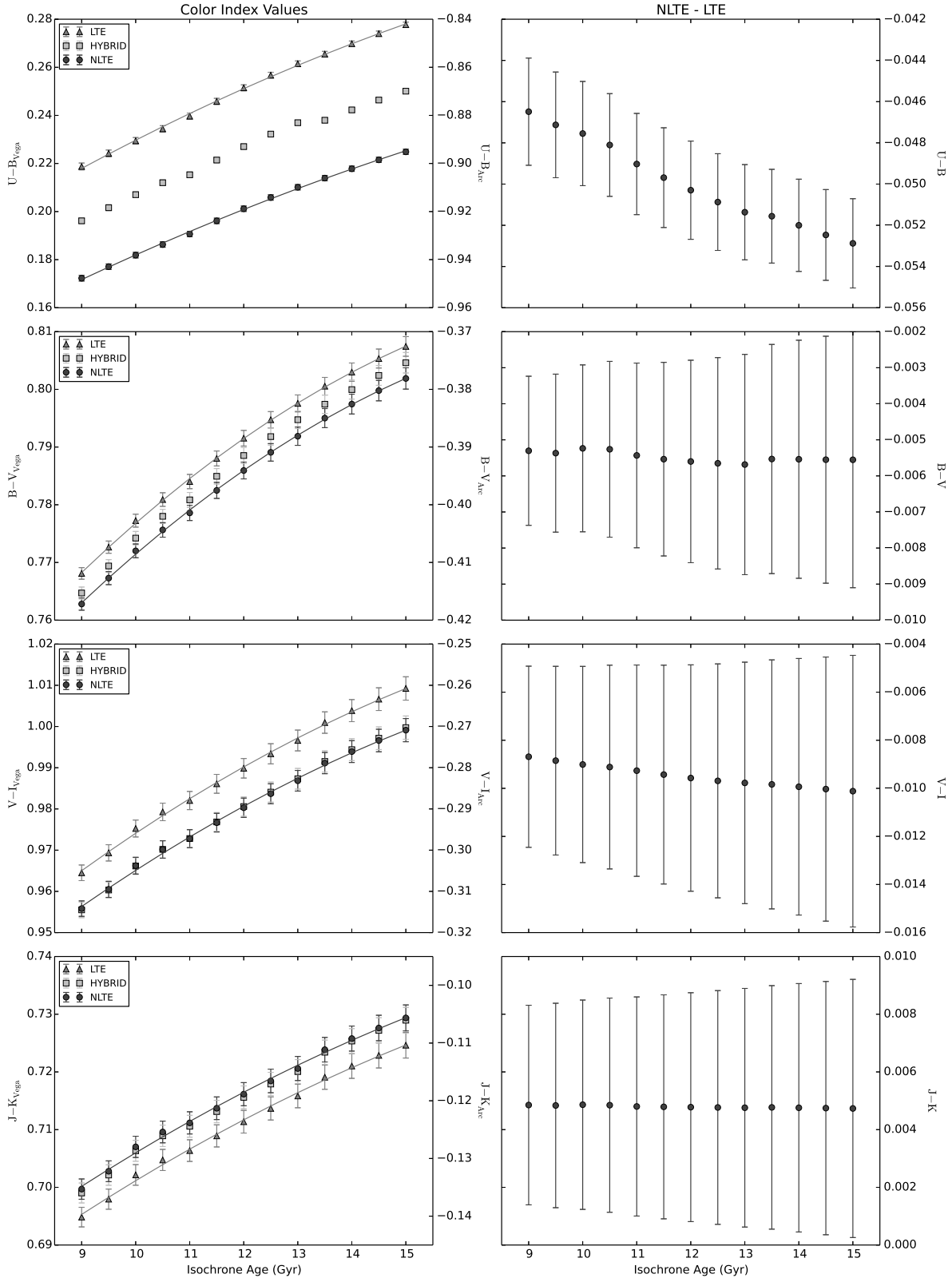


Fig. 6.— *Left Column* - Photometric colors for synthetic IL spectra of populations with constant bolometric luminosity, and  $[M/H] = -0.66$ . All populations are discretized with 25 to 35 boxes. The error bars are the CMD discretization uncertainty, outlined in Section 5.2.

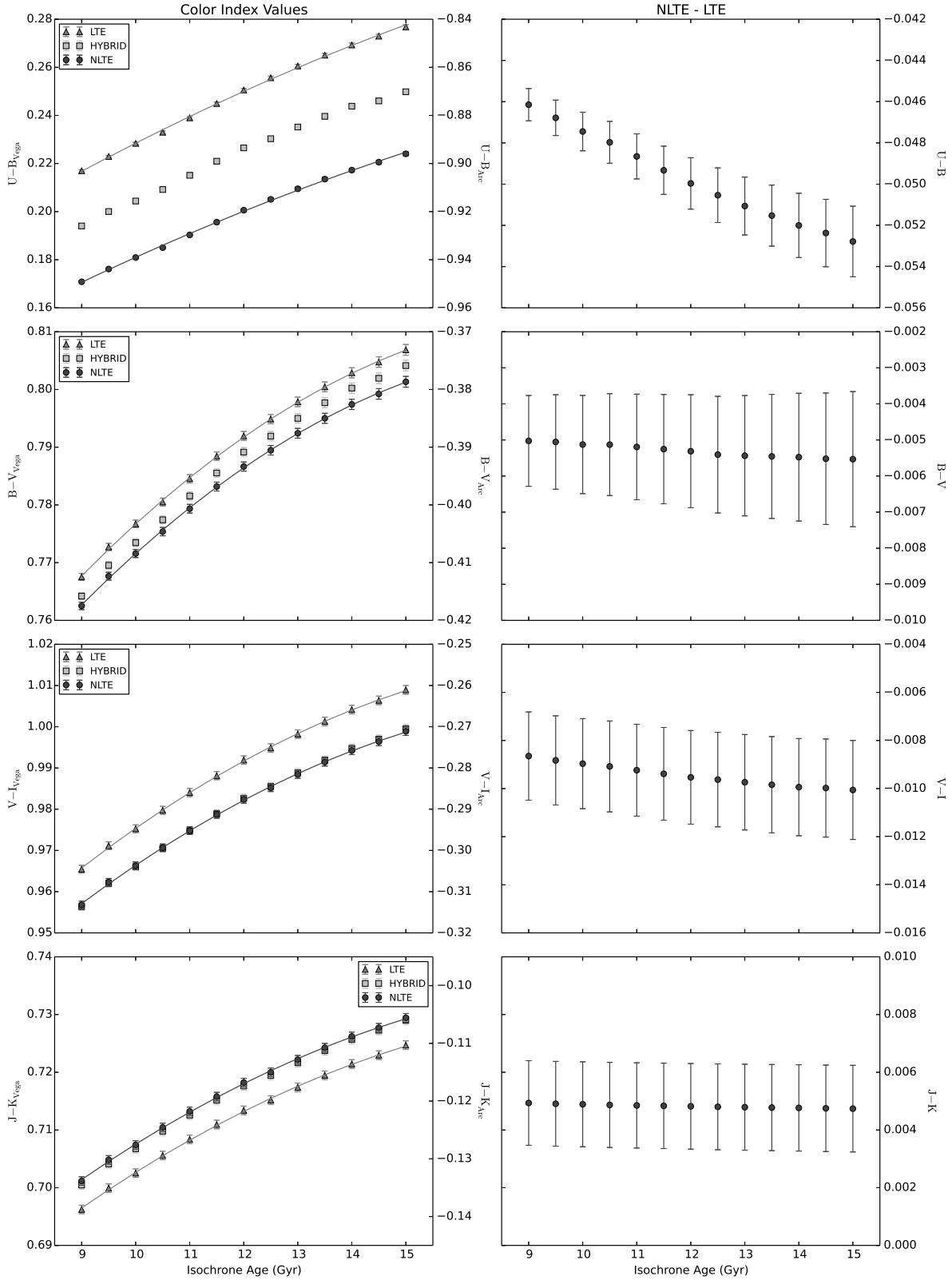


Fig. 7.— Similar to Figure 6, but for populations discretized with 40 to 50 boxes.

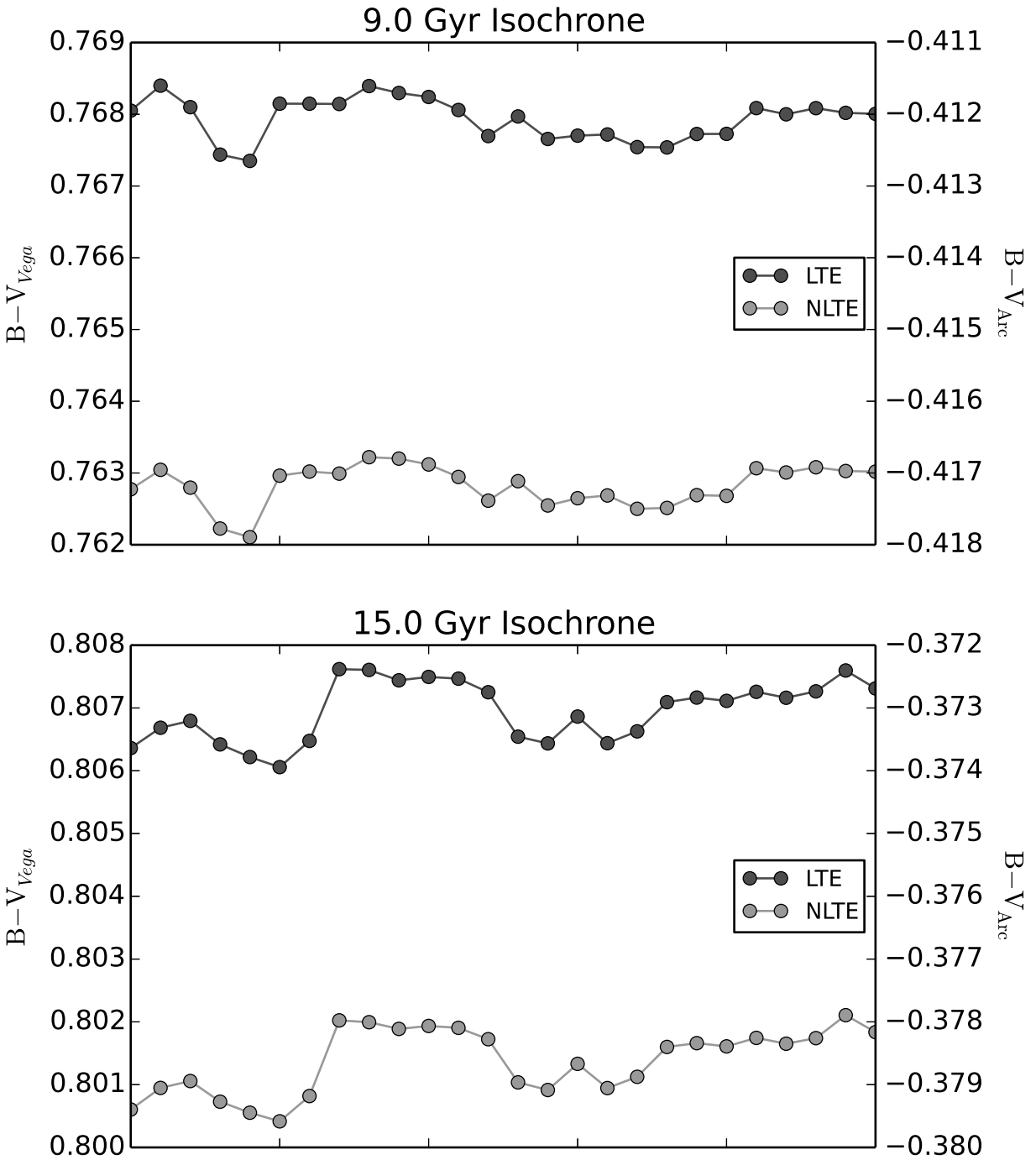


Fig. 8.— Variation of  $B - V$  color with CMD discretization resolution. *Top* - 9.0 Gyr population. *Bottom* - 15.0 Gyr population.



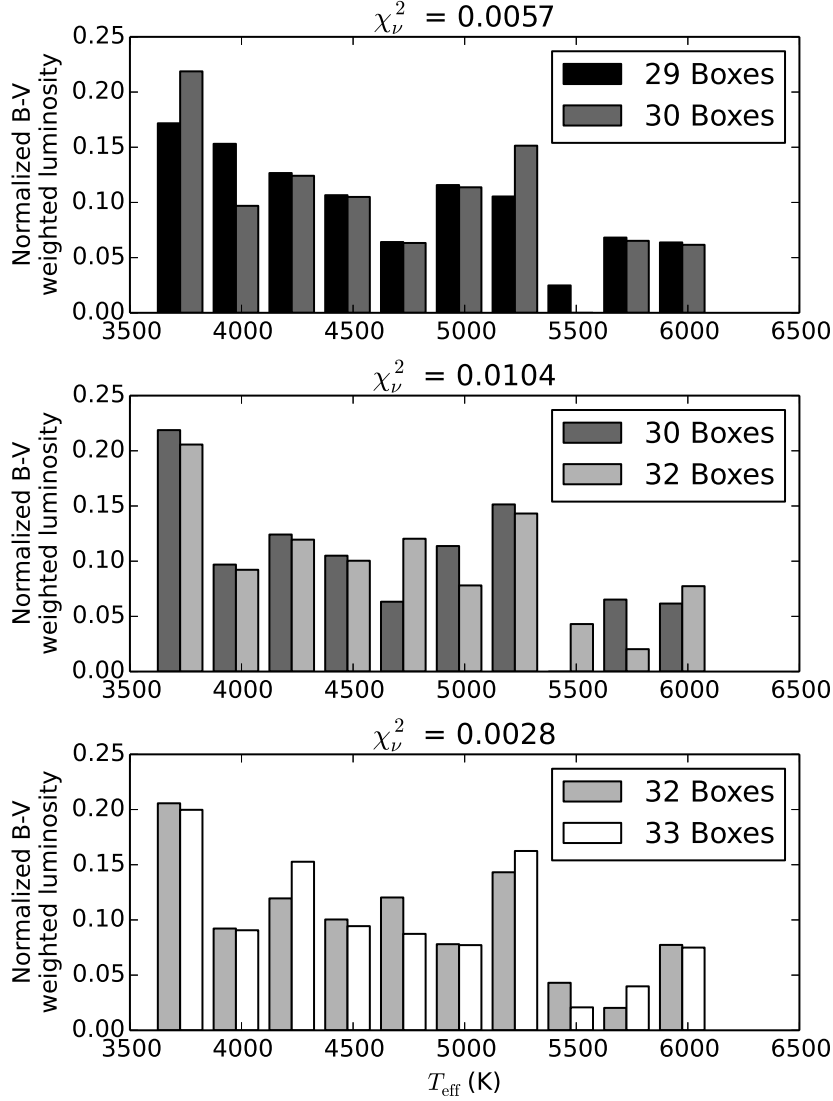


Fig. 9.— Binned representative populations for the 15.0 Gyr isochrone, with different levels of CMD discretization. The bin size is set to 250 K, the  $T_{\text{eff}}$  resolution of our library. Each bin is weighted by a factor of  $f_B/f_V$ , the flux the bin contributes to the IL spectrum in the B band divided by the flux in the V band, representing the influence each bin has on the IL B – V value. The  $\chi^2$  statistics, calculated in each case as  $\Sigma \frac{(N-n)^2}{n^2}$ , where N and n are the bin values for the sets with the greater and fewer number of boxes respectively, are used as a confirmation that the histograms in the middle panel exhibit greater differences than those in either the top or bottom panels. The middle panel, which compares discretization resolutions on either side of the large jump observed in Figure 8, shows noticeable differences in bins with  $T_{\text{eff}}$  values  $\geq 4750$  K.

Table 1. List of molecules used by PHOENIX in E.O.S. and opacity calculations. Number of isotopologues and isotopomers considered for each species included.

Molecule	Number of Isotopologues & Isotopomers	Molecule	Number of Isotopologues & Isotopomers	Molecule	Number of Isotopologues & Isotopomers
C <sub>2</sub>	3	H <sub>2</sub> O	4	NO	3
C <sub>2</sub> H <sub>2</sub>	2	H <sub>2</sub> O <sub>2</sub>	1	NO <sub>2</sub>	1
C <sub>2</sub> H <sub>6</sub>	1	H <sub>2</sub> S	3	O <sub>2</sub>	3
CH	2	H <sub>3</sub> <sup>+</sup>	1	O <sub>3</sub>	3
CH <sub>3</sub> Cl	2	HBr	2	OCS	4
CH <sub>4</sub>	5	HCN	3	OH	4
CN	4	HCl	2	PH <sub>3</sub>	1
CO	7	HF	1	SF <sub>6</sub>	1
CO <sub>2</sub>	8	HI	1	SO <sub>2</sub>	2
COF <sub>2</sub>	1	HNO <sub>3</sub>	1	SiH	3
CaH	2	HOCl	2	SiO	4
ClO	2	MgH	3	TiO	5
CrH	1	N <sub>2</sub>	1	VO	1
FeH	1	N <sub>2</sub> O	5	YO	1
H <sub>2</sub>	1	NH	2	ZrO	7
H <sub>2</sub> CO	3	NH <sub>3</sub>	2	...	...



Table 2. Comparison of old and new model atoms for atomic species treated in NLTE energy level calculations. Numbers of energy levels and b-b transitions given for each ionization stage treated in NLTE. The ground state ionization energy for each species as well as the highest energy levels in the old and new model atoms are also listed.

Species	Old Energy Levels	New Energy Levels	$\chi_I$ (eV)	$\chi_{\text{High,Old}}$ (eV)	$\chi_{\text{High,New}}$ (eV)
	/ Transitions	/ Transitions			
Li I	57/333	60/394	5.392	5.296	5.296
Li II	55/124	55/135	75.640	74.128	74.128
C I	228/1387	230/3262	11.260	11.155	11.155
N I	252/2313	254/3704	14.534	14.460	14.460
O I	36/66	146/855	13.618	12.728	13.482
Na I	53/142	58/334	5.139	5.044	5.044
Na II	35/171	35/171	47.287	45.260	45.257
Mg I	273/835	179/1584	7.646	7.644	7.634
Mg II	72/340	74/513	15.035	14.585	14.585
Al I	111/250	115/482	5.986	5.977	5.977
Al II	188/1674	191/2608	18.828	18.665	18.665
P I	229/903	230/945	10.487	10.266	10.266
P II	89/760	90/882	19.726	17.542	17.542
S I	146/349	152/1995	10.360	10.146	10.284
S II	84/444	84/501	23.334	20.375	20.375
K I	73/210	80/576	4.341	4.300	4.300
K II	22/66	22/66	31.625	27.177	27.177
Ca I	194/1029	196/2893	6.113	6.054	6.054
Ca II	87/455	89/760	11.872	11.641	11.641
Ti I	395/5279	555/13304	6.820	6.653	6.653

Table 2—Continued

Species	Old Energy Levels	New Energy Levels	$\chi_I$ (eV)	$\chi_{\text{High,Old}}$ (eV)	$\chi_{\text{High,New}}$ (eV)
	/ Transitions	/ Transitions			
Ti II	204/2399	204/2586	13.577	10.504	10.504
Mn I	316/3096	297/3067	7.435	7.418	7.418
Mn II	546/7767	512/8299	15.640	14.968	14.968
Fe I	494/6903	902/24395	7.871	7.539	7.815
Fe II	617/13675	894/22453	16.183	14.665	14.814
Co I	316/4428	364/6447	7.864	7.363	7.472
Co II	255/2725	255/2853	17.057	15.618	15.618
Ni I	153/1690	180/2671	7.635	7.422	7.422
Ni II	429/7445	670/17935	18.169	17.359	17.359
Total	6134/70492	8632/130728	...	...	...

Table 3. Error estimates in derived LTE ages caused by NLTE effects in IL spectra, and uncertainties in derived ages from our numerical uncertainty and the limiting precision of the Harris Catalog (0.01 dex) (Harris 1996) for all four color indices. Age differences are presented for the bluest and reddest color value for the LTE IL spectra for each index.

Subscripts on color indices denote which Set the estimates are associated with.

Color Index	NLTE Effect		Numerical Uncertainty		Observational Uncertainty	
	Blue	Red	Blue	Red	Blue	Red
	$U - B_1$	5.07	11.50	0.24	0.27	0.83
$U - B_2$	4.97	10.29	0.06	0.21	0.83	1.20
$B - V_1$	0.61	1.58	0.22	0.82	1.12	2.41
$B - V_2$	0.55	2.53	0.13	0.53	1.05	2.84
$V - I_1$	0.98	2.28	0.40	1.06	1.06	1.88
$V - I_2$	0.92	2.54	0.19	0.50	0.99	2.39
$J - K_1$	0.79	1.19	0.56	1.18	1.65	2.66
$J - K_2$	0.74	1.46	0.23	0.53	1.54	3.52